



Vortex shedding around a near-wall circular cylinder induced by a solitary wave



Meng-Yu Lin ^{*}, Guo-Zhen Liao

Department of Civil Engineering, Chung Yuan Christian University, Chung Li District, Taoyuan 32023, Taiwan, ROC

ARTICLE INFO

Article history:

Received 17 January 2014

Accepted 23 July 2015

Available online 8 September 2015

Keywords:

Solitary wave

Circular cylinder

Flat wall

Vortex shedding

Drag

Lift

ABSTRACT

This study developed a two-dimensional generalized vortex method to analyze the shedding of vortices and the hydrodynamic forces resulting from a solitary wave passing over a submerged circular cylinder placed near a flat seabed. Numerical results for validation are compared with other numerical and experimental results, and satisfactory agreement is found. A series of simulations were performed to study the effects of gap-to-diameter ratio and incident wave height on vorticity pattern as well as the forces exerted on the cylinder. The range of the heights of incident waves is from $0.3h$ to $0.7h$, where h is the still water depth. The range of the gap-to-diameter ratios is from 0.1 to 0.8. The results indicate that the flow pattern and the pressure distribution change significantly because of the close proximity of the seabed where the vorticity flux on the seabed-side surface of the cylinder is suppressed. Placing the cylinder nearer the seabed increases the drag and the positive lift on the cylinder. When the gap-to-diameter ratio increases, the pattern of vortices changes because of the interaction between the main recirculation zone and the shear layers separated from the gap. The maxima of drag, lift and total force increase linearly with the height of the incident wave.

© 2015 Elsevier Ltd. All rights reserved.

1. Introduction

With the development of marine engineering, installing subsea pipelines alongshore has become a common marine construction. Subsea pipeline constructions, such as those for telecommunications, power cables, crude oil transportation, running water transportation, and optical networks, are extremely relevant to people's lives. Nevertheless, waves and ocean currents in the marine environment are constantly scouring the seabed, frequently damaging subsea pipelines. For example, in 2003, a total of approximately 175 m of spanning was found in the subsea gas pipelines installed by the Chinese Petroleum Corporation (Taiwan) in the open waters of Tung Shiau, with a maximum spanning length of approximately 100 m. Subsequently, the pipelines were backfilled using the riprap method. However, an inspection conducted in 2004 found that a portion of the pipelines were again exposed and spanning, with an average spanning height of 0.4–0.5 m. Therefore, understanding the hydrodynamic phenomena surrounding subsea pipelines and the mechanism of destruction is vital in the field of marine engineering.

In addition to the pressure gradient resulting from surface waves, the creation and shedding of vortices surrounding pipelines generate significant stresses that affect subsea pipelines. When gaps occur between pipelines and the seabed, the

* Corresponding author. Tel.: +886 3 2654228; fax: +886 3 2654299.

E-mail address: mylin@cycu.edu.tw (M.-Y. Lin).

vortex effects increase in complexity. Previous studies examining this issue have yielded numerous findings regarding the flow fields of uniform and oscillating flows passing through cylinders. By contrast, few studies have simultaneously analyzed the surface waves and the vortices formed by flows passing through cylinders.

Because of the determining effects of vortices in this issue, overlooking viscous effects during analysis may limit the practicality of the results. For example, [Li and Cheng \(1999\)](#) employed potential flow theory to simulate the scour that results from unidirectional flows passing through offshore pipelines. In their study, the interactions between flow fields and topography was conducted by interaction, and the interactions among flows, pipelines, and the bed were considered. The results showed that the predicted maximum scour depths approached the depth yielded by the empirical equation only during clear-water scouring. Analysis indicated that the difference occurred because vortex effects were neglected in the potential flow model.

Because potential flow theory cannot be used to analyze vortex effects, the majority of relevant studies have applied viscous flow theory. For example, [Dipankar and Sengupta \(2005\)](#) used the stream function-vorticity formulation of the Navier–Stokes equations. They employed an improved overset grid method to simulate uniform flows passing through cylinders located above the bed, and compared the results yielded by different ratios of cylinder diameter (D) and pipeline-bed gap (G). The results showed that the lift force and drag force coefficients approached the experimental data when the G/D ratio was 0.5 and 1.5. [Liang and Cheng \(2005\)](#) used turbulence models such as the $k-\varepsilon$ model and Smagorinsky subgrid-scale model to simulate the bed scouring below a pipeline resulting from waves. In this study, waves were simulated using sinusoidal oscillatory flows; therefore, the interaction between fluctuations in the water surface and the pipelines was not analyzed. [An et al. \(2011\)](#) simulated the flow field around a cylinder near a bed boundary in oscillating flows, and used the 2D Reynolds-averaged Navier–Stokes equations and the finite element method to solve the $k-\varepsilon$ turbulence model. This study examined the flow fields surrounding cylinders when the Stokes number was 196, the KC number was between 2 and 30, and the ratio of the gap between the cylinder and the bed boundary (G/D) was between 0 and 3. The results showed that steady flow positions were affected by the KC number and the gap-to-diameter ratio.

Regarding experimental observations, [Sumer et al. \(1991\)](#) conducted an experiment that involved placing a cylinder on a plane in an oscillating flow field and examining the instantaneous pressure distribution surrounding the cylinder when the Reynolds number was relatively large ($Re = 10^5$) and the flow field of vortex motion when the Reynolds number was relatively small ($Re = 10^3\text{--}10^4$). The results indicate that vortex streets disappeared when $7 < KC < 13$. As the KC number declined, vortex shedding existed when the gap-to-diameter ratio was small, and as the gap-to-diameter ratio declined, the Strouhal frequency increased. [Lin et al. \(2005\)](#) investigated the flow fields surrounding cylinders at $Re = 780$ and the gap ratios for the planar boundary differed. The results showed that the plane had no influence on the vortex shedding frequency when $G/D > 3.0$; however, the frequency increased as the G/D declined from 3.0 to 0.6, and decreased when $G/D < 0.6$. [Qi et al. \(2006\)](#) conducted a series of experiments regarding shallow water turbulences passing through cylinders of varying height. The results indicated that unshedding occurred in the vortex structure when the cylinder contacted the bed and the free surface, and that vortex shedding occurred with variations in cylinder height. Researchers have conducted experiments to observe the scour mechanisms surrounding pipelines. For example, [Chiew \(1990\)](#) explored the primary effects that unidirectional flow fields have on the scouring mechanism. The experimental results indicated that the contact between the pipeline and stagnation eddy causes the deposition of non-cohesive soil and subsequently local scour, thereby initiating the scouring mechanism, the key factor of which is the flotation gradient of the seabed deposition. Specifically, a depth-to-diameter ratio higher than 3.5 is unlikely to result in scour. However, when the hydraulic gradient caused by the pipeline exceeds the flotation gradient of the seabed deposition, upstream stagnation eddy is likely to result in scour.

Studies examining the vortex flow fields resulting from waves passing through cylinders placed on an even seabed have rarely focused on solitary waves as the research subject. Solitary waves, which possess single peaks and infinitely long wavelengths, can be used to simulate alongshore storm surges and tsunamis. This study used solitary waves as the subject and developed a two-dimensional generalized vortex method to analyze the flow field and the hydrodynamic forces resulting from a solitary wave passing through a submerged circular cylinder placed near an even seabed. The effects that the gap between the cylinder and the seabed and the incident wave height have on vortex types and drag were also investigated.

2. Governing equations and boundary conditions

The problem of interest concerns the calculation of the two-dimensional flow of a solitary wave over a near-wall circular cylinder in a uniform channel. The viscous effects as well as the generation of vorticity at the free surface are ignored. The x -axis lies in the undisturbed free surface and the y -axis points vertically upward with unit vectors $\hat{\mathbf{e}}_x$ and $\hat{\mathbf{e}}_y$, respectively (see [Fig. 1](#)). The corresponding fluid velocity components are u and v , respectively, and \mathbf{u} is the fluid velocity vector. The motion of the fluid is governed by the incompressible Navier–Stokes equations:

$$\nabla \cdot \mathbf{u} = 0, \quad (1)$$

$$\frac{\partial \mathbf{u}}{\partial t} + \mathbf{u} \cdot \nabla \mathbf{u} = -\frac{1}{\rho} \nabla p - g \hat{\mathbf{e}}_y + \nu \nabla^2 \mathbf{u}, \quad (2)$$

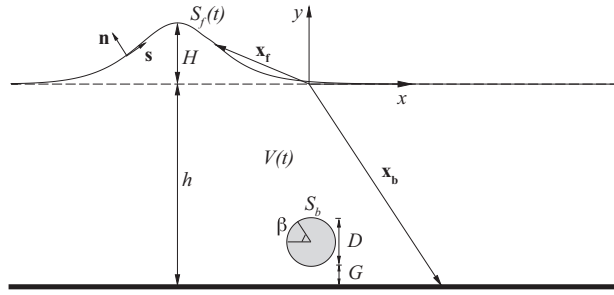


Fig. 1. Definition sketch of the problem.

where p is the fluid pressure, ρ is the density of fluid, g is the gravitational acceleration, and ν is the kinematic viscosity. In velocity–vorticity form, above equations can be expressed by the vorticity transport equation:

$$\frac{\partial \omega}{\partial t} + \mathbf{u} \cdot \nabla \omega = \nu \nabla^2 \omega, \quad (3)$$

where $\omega = \hat{\mathbf{e}}_z \cdot \nabla \times \mathbf{u}$ is the vorticity field with the unit vector $\hat{\mathbf{e}}_z$ out of the page.

At the free surface, the flow field satisfies the kinematic and dynamic boundary conditions, which can be expressed in a Lagrangian description as

$$\frac{d\mathbf{x}_f}{dt} = \mathbf{u}(\mathbf{x}_f), \quad (4)$$

$$\frac{d\mathbf{u}}{dt}(\mathbf{x}_f) = -\frac{1}{\rho} \nabla p - g \hat{\mathbf{e}}_y. \quad (5)$$

On solid boundaries (at the seabed or the boundary of the cylinder) S_b , no-slip boundary condition is employed:

$$\mathbf{u} = \mathbf{0} \quad \text{on } S_b. \quad (6)$$

3. Generalized vortex methods

3.1. Integral representation of velocity field

If the interface between air and water is not perpendicular to the pressure gradient, vorticity will be generated and must be confined to the interface at all times because of the absence of free-surface viscosity. The so-called *generalized vortex sheet* approach for interfacial waves is the basis for several different computational methods, such as those described by Longuet-Higgins and Cokelet (1976), Baker et al. (1982), Tryggvason (1988), and Lundgren and Koumoutsakos (1999) (see Marshall, 2001 for detailed description). In this research, this approach is extended to include the effect of the vorticity field generated from submerged bodies.

The flow field studied in this research is generated by the free-surface waves and the vorticity separated from the circular cylinder and the seabed. By applying the integral formulations of the Helmholtz decomposition (Lin and Huang, 2009), the integral representation for the velocity field has the form:

$$\mathbf{u}(\mathbf{x}) = \int_V \mathbf{K}(\mathbf{x} - \mathbf{x}') \omega(\mathbf{x}') d\mathbf{x}' + \int_{S_f} \mathbf{K}(\mathbf{x} - \mathbf{x}') \gamma(\mathbf{x}') d\mathbf{x}', \quad (7)$$

where V is the volume of fluid, S_f denotes the free surface, γ is the strength of a vortex sheet at the free surface, and

$$\mathbf{K}(\mathbf{x}) = \frac{1}{2\pi} \frac{\hat{\mathbf{e}}_z \times \mathbf{x}}{|\mathbf{x}|^2} = \frac{(-y, x)}{2\pi |\mathbf{x}|^2}. \quad (8)$$

In (7), the first integral represents the rotational flow field induced by vorticity, and the second integral represents the irrotational flow field induced by the vortex sheet along the free surface. The vortex sheet strength γ is related to the tangential velocity jump across the free surface:

$$\gamma = (\mathbf{u}_1 - \mathbf{u}_2) \cdot \hat{\mathbf{s}}, \quad (9)$$

where \mathbf{u}_1 and \mathbf{u}_2 are the limiting values of the velocity vector below and above the free surface, respectively, and $\hat{\mathbf{s}}$ is a unit vector oriented tangent to the vortex sheet (see Fig. 2).

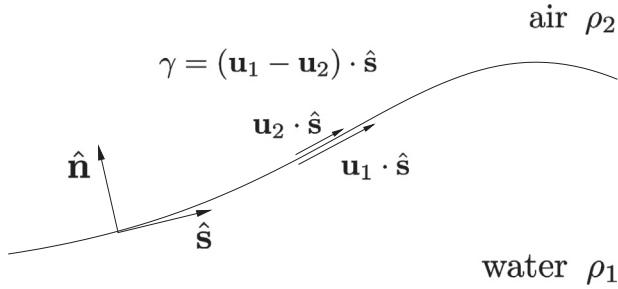


Fig. 2. Vortex sheet along the free surface.

3.2. Integro-differential formulation for free-surface waves

For brevity, here we denote water as fluid 1 and air as fluid 2, as shown in Fig. 2. The dynamic free surface boundary condition (5) for water and air can be expressed as

$$\rho_i \mathbf{a}_i = -\nabla p_i - \rho_i g \hat{\mathbf{e}}_y, \quad i = 1, 2, \quad (10)$$

where $\mathbf{a}_i = \partial \mathbf{u}_i / \partial t + \mathbf{u}_i \cdot \nabla \mathbf{u}_i$ is the acceleration of a material point in fluid i . Subtracting the tangential component of (10) across the free surface yields

$$\frac{1}{2} [(\rho_1 + \rho_2)(\mathbf{a}_1 - \mathbf{a}_2) + (\rho_1 - \rho_2)(\mathbf{a}_1 + \mathbf{a}_2)] \cdot \hat{s} = -\frac{\partial}{\partial s}(p_1 - p_2) - (\rho_1 - \rho_2)g \hat{\mathbf{e}}_y. \quad (11)$$

The velocity of the free surface, denoted by \mathbf{u}_f , has the same normal component as the fluid on either side. The tangential component of \mathbf{u}_f , which is used to advect the computational points along the vortex sheet, is arbitrary and can thus be specified in any manner that is convenient (Marshall, 2001). For simplicity, the velocity of the free surface is defined to be the average of the velocities on either side:

$$\mathbf{u}_f = \frac{1}{2}(\mathbf{u}_1 + \mathbf{u}_2), \quad (12)$$

which is equal to the principal value of the singular integral (7) when $\mathbf{x} \in S_f$. Using the definition for γ and \mathbf{u}_f we have

$$\mathbf{u}_1 = \mathbf{u}_f + \frac{1}{2}\gamma \hat{s}, \quad \mathbf{u}_2 = \mathbf{u}_f - \frac{1}{2}\gamma \hat{s}. \quad (13)$$

Following the computational points of the free surface, the Lagrangian derivative is defined such that for a function $\xi = \xi(\mathbf{x}, t)$ describing the free surface S_f ,

$$\frac{d\xi}{dt} \equiv \frac{\partial \xi}{\partial t} + (\mathbf{u}_f \cdot \nabla) \xi. \quad (14)$$

Substituting (14) into the fluid acceleration \mathbf{a}_i , we have

$$\mathbf{a}_1 = \frac{d\mathbf{u}_1}{dt} + \frac{1}{2}\gamma \frac{\partial \mathbf{u}_1}{\partial s}, \quad \mathbf{a}_2 = \frac{d\mathbf{u}_2}{dt} - \frac{1}{2}\gamma \frac{\partial \mathbf{u}_2}{\partial s}. \quad (15)$$

Here

$$\frac{d\mathbf{u}_i}{dt} = \frac{\partial \mathbf{u}_i}{\partial t} + \mathbf{u}_f \cdot \nabla \mathbf{u}_i, \quad i = 1, 2 \quad (16)$$

is the rate of change in \mathbf{u}_i on the computational points of the free surface. For simplicity, we define the average acceleration over the free surface as

$$\mathbf{a}_f \equiv \frac{1}{2}(\mathbf{a}_1 + \mathbf{a}_2). \quad (17)$$

One may notice that \mathbf{a}_f is not the acceleration of free-surface points. The relation between the average acceleration \mathbf{a}_f and the acceleration of free-surface points $d\mathbf{u}_f/dt$ can be shown using (12)–(17) as

$$\mathbf{a}_f \cdot \hat{s} = \frac{d\mathbf{u}_f}{dt} \cdot \hat{s} + \frac{1}{8} \frac{\partial(\gamma^2)}{\partial s}. \quad (18)$$

Dividing (11) by $\rho_1 + \rho_2$, using the above definitions and ignoring the effect of surface tension, we obtain the equation governing the evolution of the vortex sheet strength γ :

$$\frac{d\gamma}{dt} + \gamma \frac{\partial \mathbf{u}_f}{\partial s} \cdot \hat{s} = 2A\mathbf{a}_f \cdot \hat{s} + 2Ag \hat{\mathbf{e}}_y \cdot \hat{s}, \quad (19)$$

where $A = (\rho_1 - \rho_2)/(\rho_1 + \rho_2)$ is the Atwood ratio. Substituting (18) for the $\mathbf{a}_f \cdot \hat{s}$ term into (19) and evaluating \mathbf{u}_f by the Biot-Savart equation (7) yields an integro-differential equation for the evolution of the vortex sheet strength γ .

From the integral representation shown in (7) with the vorticity transport equation (3) and the evolution equation for γ (19), an alternative problem can be constructed for solving \mathbf{x}_f , ω and γ rather than the original problem with primitive variables \mathbf{x}_f , \mathbf{u} and p . The flow field evolves by following the trajectories of the vorticity-carrying elements \mathbf{x}_ω and the free-surface points \mathbf{x}_f , and then updating their strengths based on the following sets of equations. For vorticity ω ,

$$\frac{d\mathbf{x}_\omega}{dt} = \mathbf{u}, \quad (20a)$$

$$\frac{d\omega}{dt} = \nu \nabla^2 \omega, \quad (20b)$$

and for vortex sheet γ ,

$$\frac{d\mathbf{x}_f}{dt} = \mathbf{u}_f, \quad (21a)$$

$$\frac{d\gamma}{dt} = -\gamma \frac{\partial \mathbf{u}_f}{\partial S} \cdot \hat{\mathbf{s}} + 2A\mathbf{a}_f \cdot \hat{\mathbf{s}} + 2A\mathbf{g}\hat{\mathbf{e}}_y \cdot \hat{\mathbf{s}}. \quad (21b)$$

3.3. Lagrangian vortex particle method for vorticity field

The vorticity field ω is determined by applying a Lagrangian vortex particle method (VPM) to obtain a numerical approximation in terms of N vorticity-carrying particles:

$$\omega(\mathbf{x}, t) = \sum_{j=1}^N \eta_e(\mathbf{x} - \mathbf{x}_j(t)) \Gamma_j(t). \quad (22)$$

Each particle is identified by its position, \mathbf{x}_j , and its circulation, Γ_j . The regularized function η_e is the Gaussian distribution:

$$\eta_e(\mathbf{x}) = \frac{1}{2\pi\epsilon^2} \exp\left(-\frac{|\mathbf{x}|^2}{2\epsilon^2}\right). \quad (23)$$

Here the quantity ϵ is the core size of the vortex particles. According to (20a) and (20b), the vorticity field is solved by transporting the particles in a Lagrangian frame, and accounting for viscous effects by changing their strength.

To handle the generation of vorticity from the solid boundary S_b , a typical time interval $[t, t+\delta t]$ is divided into two substeps.

- In substep 1, we solve the positions and the strengths of the discretized vortex sheet at the free surface and the existing vorticity-carrying particles. By applying (7) and (22), the local velocity employed in (20a), (21a) and (21b) can be expressed as

$$\mathbf{u}(\mathbf{x}_j) = \sum_{i=1}^N \mathbf{K}_e(\mathbf{x}_j - \mathbf{x}_i) \Gamma_i + \int_{S_f} \mathbf{K}(\mathbf{x}_j - \mathbf{x}) \gamma(\mathbf{x}) d\mathbf{x}, \quad (24)$$

where

$$\mathbf{K}_e(\mathbf{x}) = \mathbf{K}(\mathbf{x}) \left[1 - \exp\left(-\frac{|\mathbf{x}|^2}{2\epsilon^2}\right) \right]. \quad (25)$$

The diffusion of the vorticity field, (20b), is implemented by the technique of particle strength exchange (Dedond and Mas-Gallic, 1989) with a Gaussian cut-off function. For the i -th particle, the rate of change of its circulation is

$$\frac{d\Gamma_i}{dt} \Big|_{PSE} = \nu \frac{2}{\epsilon^2} \sum_{j=1}^N (S_i \Gamma_j - S_j \Gamma_i) \eta_e(\mathbf{x}_i - \mathbf{x}_j), \quad (26)$$

where S_i is the area of fluid associated with the particle. After this substep, a slip velocity is present at S_b .

- In substep 2, a spurious vortex sheet at S_b , γ_b , necessary to cancel the slip velocity generated by substep 1 is solved, and then the circulation of vortex particles near S_b is updated due to the viscous diffusion of γ_b . The velocity jump caused by γ_b leads to the no-slip condition, $\mathbf{u} \cdot \hat{\mathbf{s}} = 0$, on the solid wall. Since the velocity on the solid wall with the vortex sheet γ_b is

$$\mathbf{u}(\mathbf{x}) = \frac{1}{2} \gamma_b(\mathbf{x}) \hat{\mathbf{s}} + PV \int_{S_b} \mathbf{K}(\mathbf{x} - \mathbf{x}') \gamma_b(\mathbf{x}') d\mathbf{x}' + \sum_j \mathbf{K}_e(\mathbf{x} - \mathbf{x}_j) \Gamma_j + \int_{S_f} \mathbf{K}(\mathbf{x} - \mathbf{x}') \gamma_f(\mathbf{x}') d\mathbf{x}', \quad \mathbf{x} \in S_b, \quad (27)$$

where PV denotes the Cauchy principal value of the integral, the no-slip condition gives the integral equation for solving γ_b :

$$\frac{1}{2} \gamma_b(\mathbf{x}) + PV \int_{S_b} \hat{\mathbf{s}}(\mathbf{x}) \cdot \mathbf{K}(\mathbf{x} - \mathbf{x}') \gamma_b(\mathbf{x}') d\mathbf{x}' = -\hat{\mathbf{s}}(\mathbf{x}) \cdot \left[\sum_j \mathbf{K}_e(\mathbf{x} - \mathbf{x}_j) \Gamma_j + \int_{S_f} \mathbf{K}(\mathbf{x} - \mathbf{x}') \gamma_f(\mathbf{x}') d\mathbf{x}' \right]. \quad (28)$$

This spurious vortex sheet is then diffused into the fluid by solving the diffusion equation with the Neumann-type boundary condition (Koumoutsakos et al., 1994):

$$\nu \frac{\partial \omega}{\partial n} \approx -\frac{\gamma_b}{\delta t}. \quad (29)$$

Consider a uniform strength γ_b distributed along a panel with length l , the solution of the Neumann-type diffusion equation distributes the circulation caused by γ_b to a neighbor particle at \mathbf{x}_i in the form

$$\left. \frac{dI_i}{dt} \right|_{\text{wall}} = \frac{\gamma_b(\mathbf{x}')}{\delta t} \int \int_{S_i} \phi(\mathbf{x}_i - \mathbf{x}', \delta t) dx dy, \quad (30)$$

with

$$\phi(\mathbf{x}, t) = \frac{1}{\sqrt{4\pi\nu\delta t}} \exp\left(-\frac{x_n^2}{4\nu\delta t}\right) [\operatorname{erfc}(\xi)]_{(x_s-l/2)/\sqrt{4\nu\delta t}}^{(x_s+l/2)/\sqrt{4\nu\delta t}}, \quad (31)$$

where $x_n = \mathbf{x} \cdot \hat{\mathbf{n}}$ and $x_s = \mathbf{x} \cdot \hat{\mathbf{s}}$. For a detailed description of evaluating the integral in (30), see Ploumhans and Winckelmans (2000). At the end of the time interval, the total rate of change of circulation is

$$\frac{dI_i}{dt} = \left. \frac{dI_i}{dt} \right|_{\text{PSE}} + \left. \frac{dI_i}{dt} \right|_{\text{wall}}. \quad (32)$$

Considering the stability of the computation for the free-surface motion, a fourth-order Adams–Bashforth–Moulton predictor–corrector scheme is used to perform the time integration for $d\gamma_f/dt$ and $d\mathbf{x}_f/dt$. Because that a redistribution technique (see Section 3.4) needs to be performed every time step, the time marching of the position and the strength of each vortex particle is achieved using the Euler forward method. Therefore, the stability of computation is constrained by the vortex particle computation. A detailed description of the solution procedure can be found in Lin and Huang (2009).

3.4. Other numerical implementation

To preserve the accuracy in the PSE scheme, one needs to maintain the condition that the particle cores overlap at all times. It is necessary to interpolate the vorticity field with distorted locations onto equispaced particle locations. If the core radius is spatially varying, the remeshing is performed in a mapped domain in which the vorticity is interpolated onto a 1×1 mapped lattice. To achieve this, a remeshing scheme with the third-order M_4 interpolation kernel introduced by Monaghan (1985) is used. In the vicinity of boundaries, the decentered A'_p kernels, which conserve up to order $p \leq 3$ of the vorticity distribution, are used instead (see Ploumhans and Winckelmans, 2000). In the computations presented in Section 6, an artificial viscosity model (Cottet, 1996), regarded as an eddy viscosity model in vortex methods, is adopted to cancel the contribution from the antidiffusive part of the truncation error involved in vortex computations.

4. Calculation of hydrodynamic force

The hydrodynamic force can be computed as the sum of pressure force \mathbf{F}_p and the friction force \mathbf{F}_f as

$$\mathbf{F}_p = - \int_{S_b} p \hat{\mathbf{n}} dS, \quad \mathbf{F}_f = \int_{S_b} \tau_s \hat{\mathbf{s}} dS, \quad (33)$$

where τ_s is the shear stress acting on the wall of the cylinder. From the Navier–Stokes equation in the following form:

$$\rho \frac{D\mathbf{u}}{Dt} = -\nabla p - \mu \nabla \times (\boldsymbol{\omega} \hat{\mathbf{e}}_z)$$

one may find that on a stationary solid surface, vorticity diffusion flux is generated due to a pressure gradient as

$$\mu \frac{\partial \omega}{\partial n} = \frac{\partial p}{\partial s}. \quad (34)$$

Therefore, pressure on the cylinder can be determined from the surface integral of the flux of vorticity, and the total pressure force acting on the cylinder is given by

$$\mathbf{F}_p = -R \int_0^{2\pi} p(\theta) \hat{\mathbf{n}} d\theta = -R^2 \int_0^{2\pi} \left[\int_0^\theta \mu \frac{\partial \omega}{\partial n}(\theta') d\theta' \right] \hat{\mathbf{n}} d\theta \quad (35)$$

where R is the radius of the circular cylinder. The vorticity flux is from the enforcement of the no-slip boundary condition, as discussed in [Section 3.3](#). Shear stress acting on the wall of the cylinder can be expressed in terms of the wall vorticity as

$$\tau_s = -\mu\omega, \quad (36)$$

and the total friction force on the cylinder

$$\mathbf{F}_f = -R \int_0^{2\pi} \mu\omega \hat{\mathbf{s}} d\theta. \quad (37)$$

The vorticity on the cylinder is computed by the numerical evaluation of the Laplacian of the streamfunction, which is discussed in [Koumoutsakos and Leonard \(1995\)](#).

The total force on the cylinder $\mathbf{F}_b = \mathbf{F}_p + \mathbf{F}_f$. The drag, lift and resultant force coefficients of the cylinder, c_D , c_L and c_T respectively, are given by

$$c_D = \frac{\mathbf{F}_b \cdot \hat{\mathbf{e}}_x}{\rho U^2 R}, \quad c_L = \frac{\mathbf{F}_b \cdot \hat{\mathbf{e}}_y}{\rho U^2 R}, \quad c_T = \frac{(\mathbf{F}_b \cdot \mathbf{F}_b)^{1/2}}{\rho U^2 R}, \quad (38)$$

where U is the characteristic velocity of the flow.

5. Model validation

To validate the present model, several numerical tests were conducted, and the results were compared with the experimental data and the numerical results computed by other schemes. All tests revealed that the present model can accurately simulate the interaction of a solitary wave and a submerged obstacle, and the flow past a circular cylinder closed to a flat wall.

5.1. Interaction of a solitary wave and a submerged semicircular cylinder

The interaction of a solitary wave and a submerged semicircular cylinder placed on a flat bottom was modelled by the present model. The computational results are compared with the experimental records of [Cooker et al. \(1990\)](#) to validate the accuracy of the computations of surface waves. In this simulation, the water depth $h=1$, the cylinder radius $R=0.6$, the incident wave height $H=0.311$, and the computational domain is $-25 \leq x \leq 25$. The time step used is $\delta t=0.01$, and the number of panels is 780 at the free surface and 200 on the surface of the cylinder. [Fig. 3](#) shows the computational profiles of the solitary wave and the wave records at three gauges. The experimental records measured by [Cooker et al. \(1990\)](#) are also presented in [Fig. 3\(b\)](#). The overall agreement is good. Small discrepancies occur after $t=12$, by which time the crest has been away from the obstacle. Because the top of the obstacle is closed to the free surface, the separated vortices from the obstacle lead to small-scale disturbances. The discrepancies between numerical and experimental results can be attributed to the three-dimensional effect of the vortices, which is not modelled in the present computation.

5.2. Impulsively started circular cylinder

To validate the calculation of vorticity field as well as the associated drag coefficient, the flows induced by an impulsively started circular cylinder (without free surface and seabed) at Reynolds number $Re=550$ and 9500 are simulated. The Reynolds number of the flow is defined based on the diameter of the cylinder ($2R$, where R is the radius of the cylinder) and the velocity of the cylinder (U_0). In the computations, the time step used is $\delta t=0.01$, and the number of panels on the cylinder surface is 300 for $Re=550$ and 1000 for $Re=9500$.

5.2.1. $Re=550$

[Fig. 4](#) shows the comparison for the equivorticity lines for $Re=550$ at $t(U_0/R)=1, 3, 5$ and 7 obtained by the present model and those by [Koumoutsakos and Leonard \(1995\)](#). [Fig. 5](#) shows the instantaneous streamlines at $t(U_0/R)=5$ computed by (a) the present model, (b) by [Smith and Stansby \(1988\)](#) using a vortex-in-cell method, and (c) by [Chang and Chern \(1991\)](#) using a so-called deterministic vortex method. The experimental result of the streaklines obtained by [Bouard and Coutanceau \(1980\)](#) is also presented for comparison. These results are in good agreement.

In [Fig. 6](#) the drag coefficient obtained by the present model is compared with the results of [Koumoutsakos and Leonard \(1995\)](#) and [Chang and Chern \(1991\)](#). The overall agreement is good, but the present result is in better agreement with that of [Koumoutsakos and Leonard \(1995\)](#). In [Fig. 7](#), the evolution of the pressure and friction drag coefficient as well as the total drag is presented. In this figure, the total drag is computed by using two methods. One is the sum of the pressure and friction drag, and the other is computed by the time derivative of the linear impulse of vorticity in the fluid as

$$\mathbf{F}_b = -\frac{d}{dt} \int_V \boldsymbol{\omega} \times \mathbf{x} d\mathbf{x} = \frac{d}{dt} \sum_{j=1}^N \Gamma_j \mathbf{x}_j \times \hat{\mathbf{e}}_z.$$

As shown in [Fig. 7](#), two methods exhibit identical results.

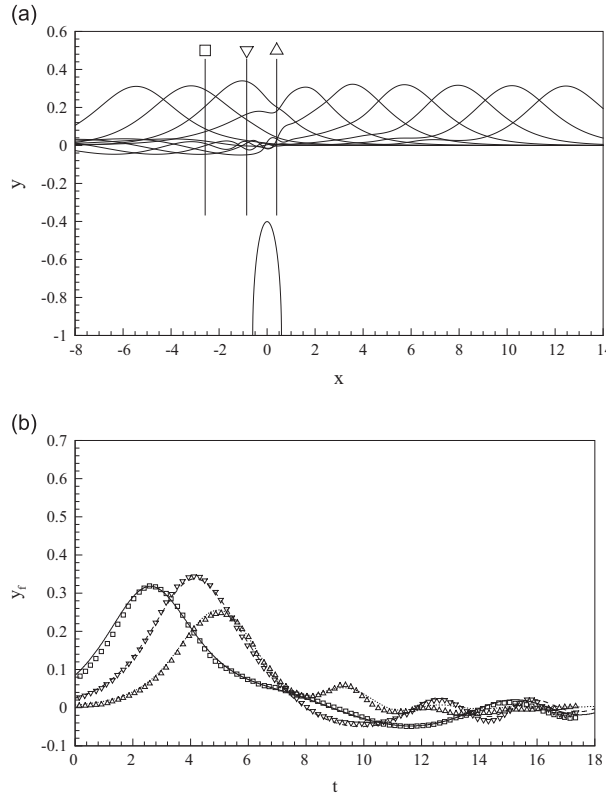


Fig. 3. (a) Computed profiles of a solitary wave passing over a semicircular cylinder at $t = 0, 2, 4, 6, \dots, 16$, and the positions of experimental wave gauges conducted by Cooker et al. (1990). The symbol over each gauge corresponds to the symbol used in (b) to plot the gauge's record. (b) Comparisons of experimental wave gauge records (\square , ∇ , and \triangle) conducted by Cooker et al. (1990) with the present computations (—, - - -, and ...). Time increases along the x -axis in units of $(h/g)^{1/2}$.

5.2.2. $Re=9500$

In Fig. 8, the vorticity field and instantaneous streamlines computed by the present model for an impulsively started cylinder at $Re=9500$ and $t(U_0/R)=2.0$ are presented and compared with the experimental result of Bouard and Coutanceau (1980). Fig. 9 shows the comparison of the drag coefficients computed by several methods, including the present model, the vortex method by Koumoutsakos and Leonard (1995), the finite difference method by Wu et al. (1994), and the deterministic vortex method by Chang and Chern (1991). Except the result of Chang and Chern (1991), all results are in good agreement. It seems that the relatively low resolution using in Chang and Chern (1991) causes this discrepancy (Koumoutsakos and Leonard, 1995).

5.3. Moving cylinder above a plane boundary

The flow past a circular cylinder moving at different heights above a plane no-slip boundary is simulated for $Re=200$. Three gap heights are considered: $G/D = 0.1, 0.5$ and 2.0 . The computational results are compared with those of Rao et al. (2013) using a spectral-element method. In the computations, a circular cylinder of diameter $D=1.0$ is located at $x=0$. The computational domain is $-3.0 \leq x \leq 30$. The time step used in the computation is $\delta t = 0.01$, and the number of panels on the cylinder surface is 100. Fig. 10 shows the vorticity fields of different gap heights at instant of maximum lift coefficient in the shedding cycle. The left half of the figure shows the present results, and the right half shows the results of Rao et al. (2013). The flow structures computed by the two models are in good agreement. For the cylinder moving at a small gap height, a single recirculation zone forms in the wake, and vortex shedding is suppressed by the effect of the wall. For the cylinder moving at larger gap heights, the secondary vortex formed behind the cylinder becomes more obvious, and the wake behaves as the formation of von Kármán vortex street.

6. Results and discussion

This section presents the computational results concerning the flow around a submerged circular cylinder above a flat seabed and is attacked by a solitary wave. The computations are nondimensionalized with the still water depth h as the

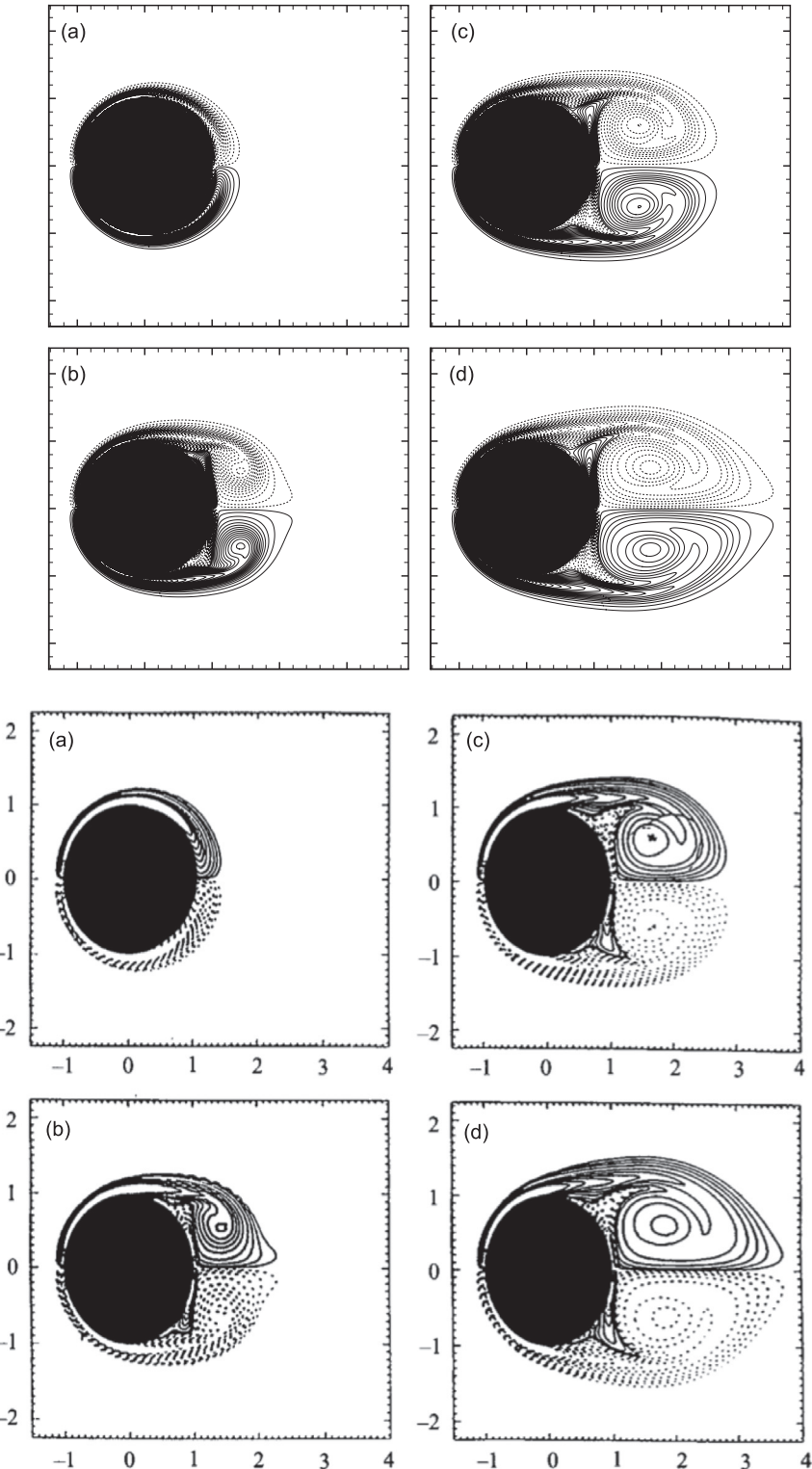


Fig. 4. Vorticity contours for an impulsively started circular cylinder at $\text{Re}=550$. (a-d) Time $t(U_0/R)=1, 3, 5, 7$ respectively. The top half is the present computational results, and the bottom half is the computational results of [Koumoutsakos and Leonard \(1995\)](#).

length scale and the linear long-wave phase speed $U=\sqrt{gh}$ as the velocity scale. In all cases the diameter of the cylinder $D=0.2h$. Computations are performed for various values of G/D and H/h ratios, where G is the gap height and H is the incident wave height (see Fig. 1). The effect of Reynolds number is not discussed in this research, and in all cases we set

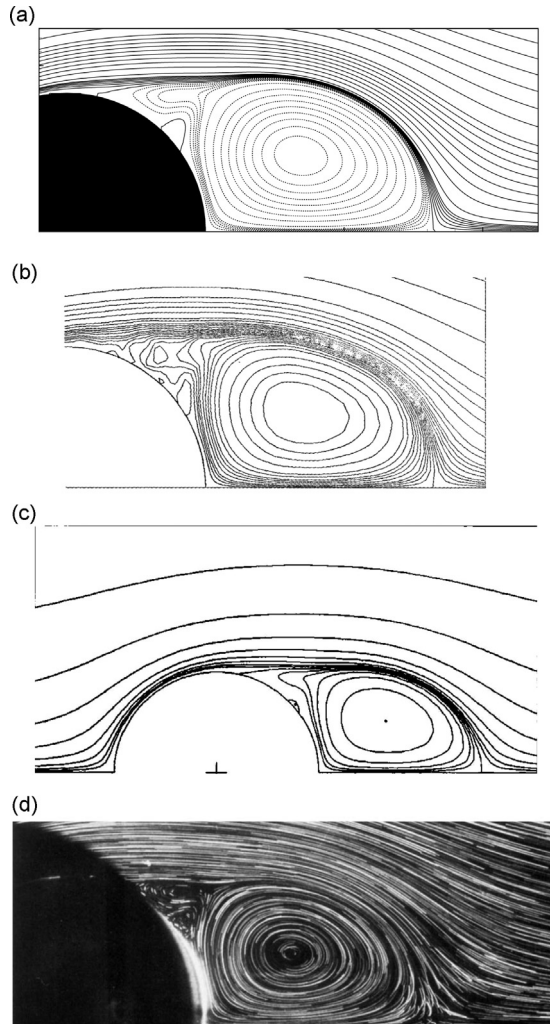


Fig. 5. Computational results of (a) the present model, (b) Smith and Stansby (1988), and (c) Chang and Chern (1991) for an impulsively started circular cylinder for $\text{Re}=550$ at $t(U_0/R)=5$. (d) is the experimental result of Bouard and Coutanceau (1980).

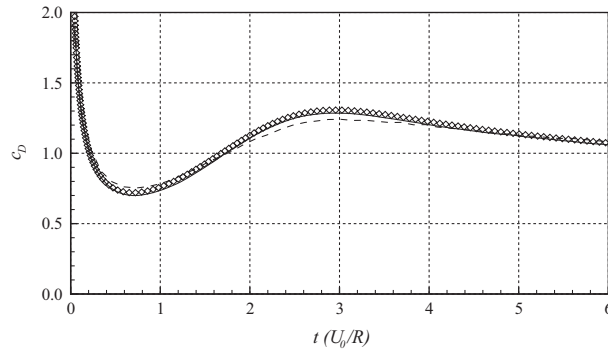


Fig. 6. Comparison of the drag coefficient of an impulsively started circular cylinder at $\text{Re}=550$ as computed by several numerical schemes: \diamond , present; —, Kouroutsakos and Leonard (1995); and ---, Chang and Chern (1991).

$\text{Re}=10\,000$. The initial wave profile is obtained using Tanaka's method (see Lin and Huang, 2009). Because the limit of the initial wave height obtained is $H/h \leq 0.7874$, the cases with wave height $H/h = 0.3, 0.4, 0.5, 0.6$, and 0.7 were computed.¹

¹ A detailed investigation of the almost-highest solitary waves was provided by Longuet-Higgins and Fox (1996).

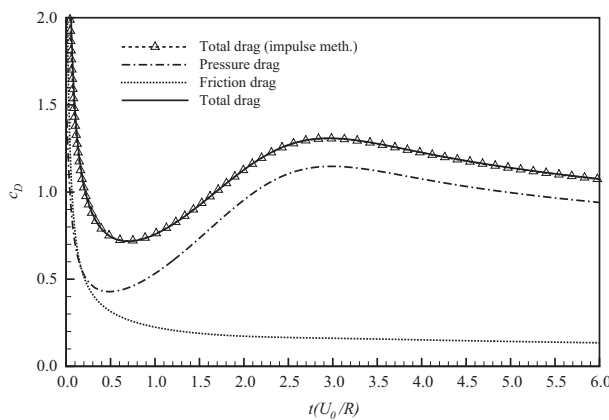


Fig. 7. Evolution of the pressure and friction drag coefficient for an impulsively started circular cylinder at $\text{Re}=550$.

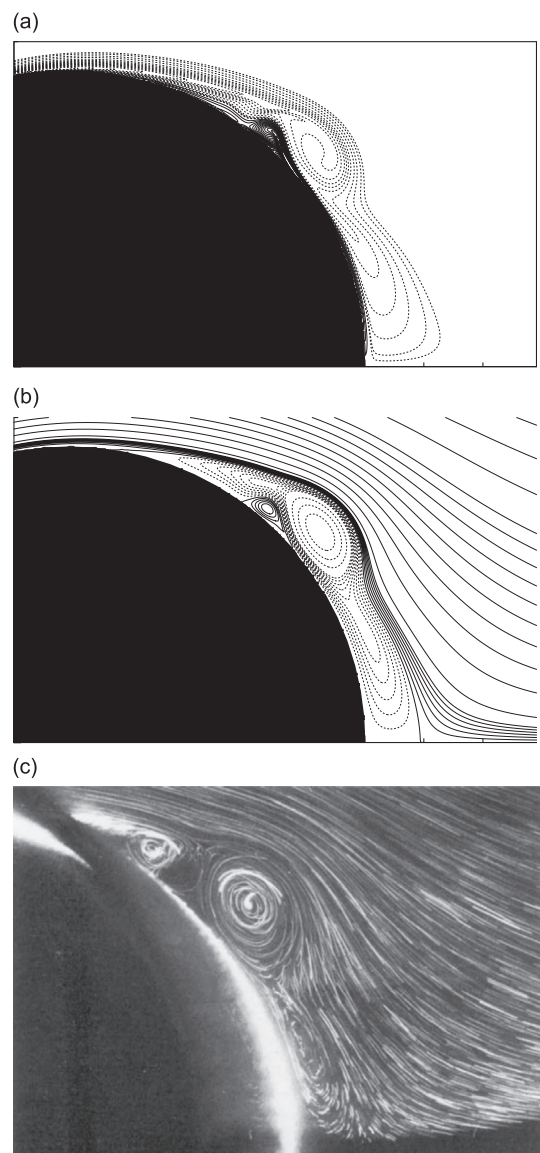


Fig. 8. (a) Equipotential lines and (b) instantaneous streamlines from computations and (c) experiments (Cooker et al., 1990) for $\text{Re}=9500$, $t(U_0/R)=2.0$.

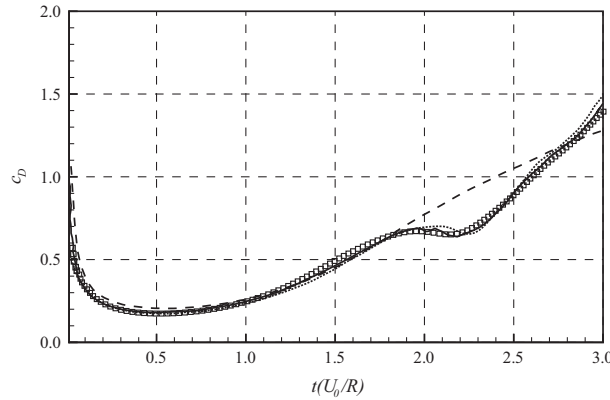


Fig. 9. Comparison of the drag coefficient of an impulsively started circular cylinder at $\text{Re}=9500$, as computed by various numerical schemes: □, present; —, Koumoutsakos and Leonard (1995);, Wu et al. (1994); and ---, Chang and Chern (1991).

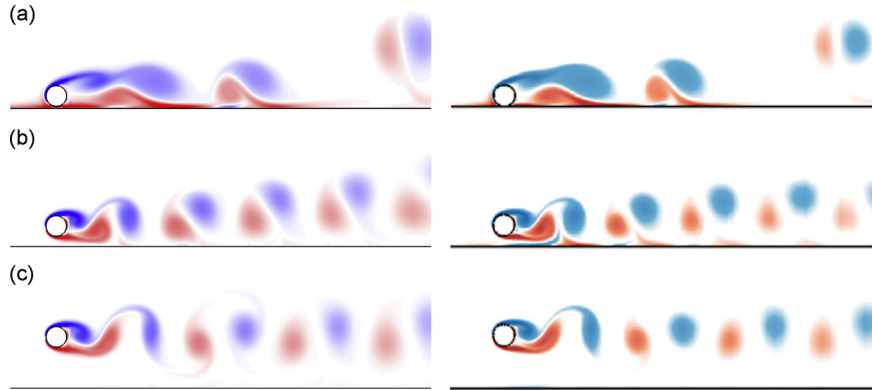


Fig. 10. Vorticity fields at $\text{Re}=200$ for the circular cylinder moving above a plane boundary at the specified gap heights. Left: present results; right: results of Rao et al. (2013). (a) $G/D = 0.1$. (b) $G/D = 0.5$. (c) $G/D = 2.0$.

In all computations, the domain is $-25 \leq x \leq 25$, the time step is $\delta t = 0.01$, and the number of panels is 800 at the free surface and 400 on the surface of the cylinder. The maximum number of particles used in the computations is about 100 000. In all the results presented, the figures are given in terms of nondimensional quantities.

6.1. Profiles of solitary waves

Fig. 11 shows the time evolution of free-surface profiles for $H/h = 0.3$ and the gap heights $G/D = 0.1$ and 3.0 . Because the diameter of the cylinder is relatively small, the disturbance of free surface due to the cylinder is weak, even in the case of larger gap height. Therefore, the deformation of solitary waves is not discussed here. Fig. 12 shows the time evolution of free-surface elevation above the cylinder for $G/D = 0.1$ and all the H/h values. In all cases, initial wave crests are at the same position ($x \approx -17$), but higher wave propagates faster. This figure identifies the relationship between time t and the free-surface elevation above the cylinder, which would be helpful for identifying the wave elevation near the cylinder in the following figures.

6.2. Vorticity patterns

6.2.1. Effect of gap height for $H/h = 0.3$

To discuss the effect of gap-to-diameter ratio on vorticity patterns, in Fig. 13 the computational results for $H/h = 0.3$ with $G/D = 0.1, 0.3, 0.5$ and 0.8 are presented. In the case of $G/D = 0.1$, because the cylinder is in close proximity to the seabed, the shear layer within the gap has no significant effect on the overall vorticity field. As the driving flow increases during the approach of the wave crest, the separated shear layer from the upper half of the cylinder rolls up and forms a recirculating

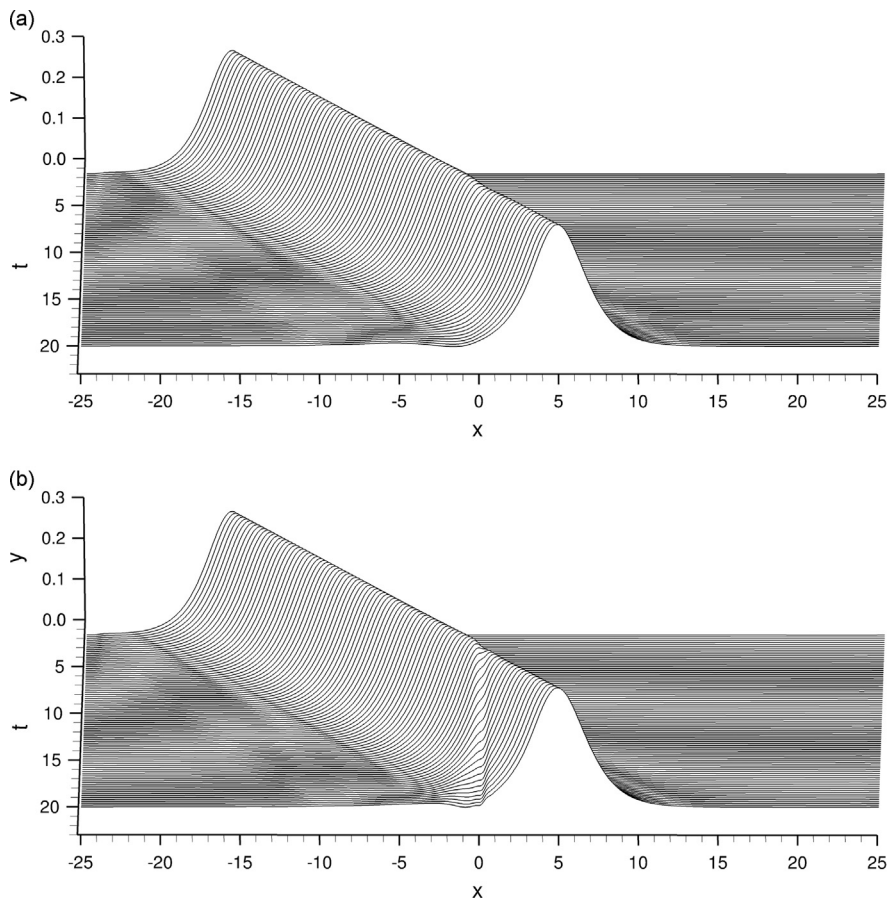


Fig. 11. Free-surface profiles at various times for $H/h = 0.3$. (a) $G/D = 0.1$. (b) $G/D = 3.0$.

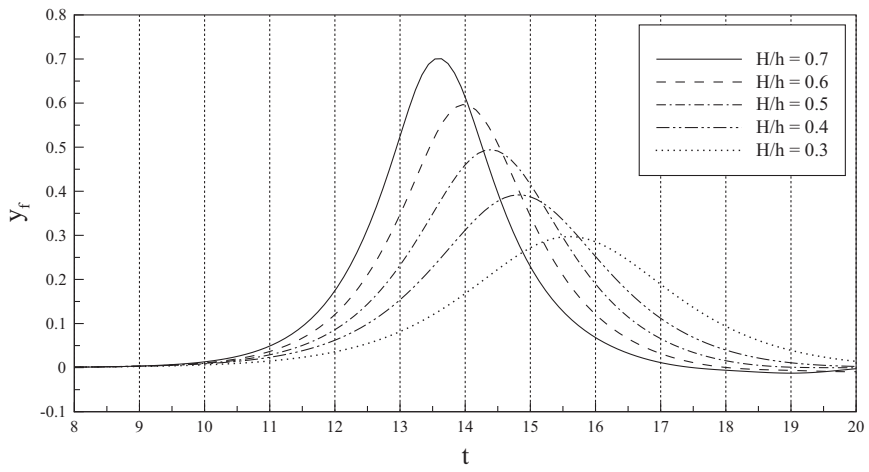


Fig. 12. Evolution of the free-surface elevation above the circular cylinder for $G/D = 0.1$ and the specified wave heights.

region as the main vortex with negative (clockwise) vorticity behind the cylinder. With the leaving of the wave crest ($t \geq 18$), the irrotational flow field gradually weakens and the vortical flow becomes dominant. This leads to the spread of the main vortex, and then the secondary vorticity (counterclockwise) vertically penetrates the main shear layer from the cylinder.

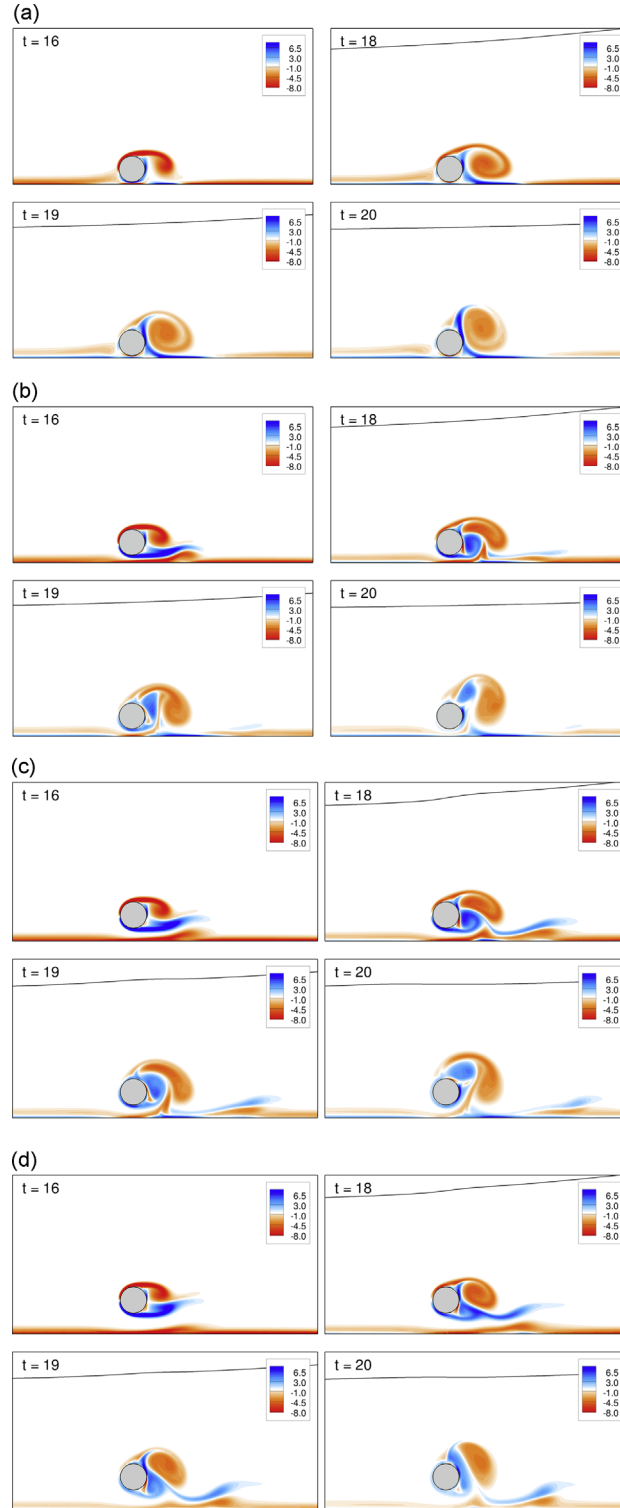


Fig. 13. Vorticity fields for $H/h = 0.3$ at the specified gap heights. (a) $G/D = 0.1$. (b) $G/D = 0.3$. (c) $G/D = 0.5$. (d) $G/D = 0.8$.

In the case of $G/D = 0.3$, due to the increased gap height, the secondary vortex stretches out along the seabed before the wave crest is away from the cylinder, as seen at $t=16$. When the wave crest moves farther, as shown at $t=18$, the stretching secondary vortex along the seabed is cut off by the negative vorticity. As the irrotational flow field gradually ceases (see $t=19$ and 20), the primary vortex and the surrounded secondary vortex act like a vortex dipole and then move upward.

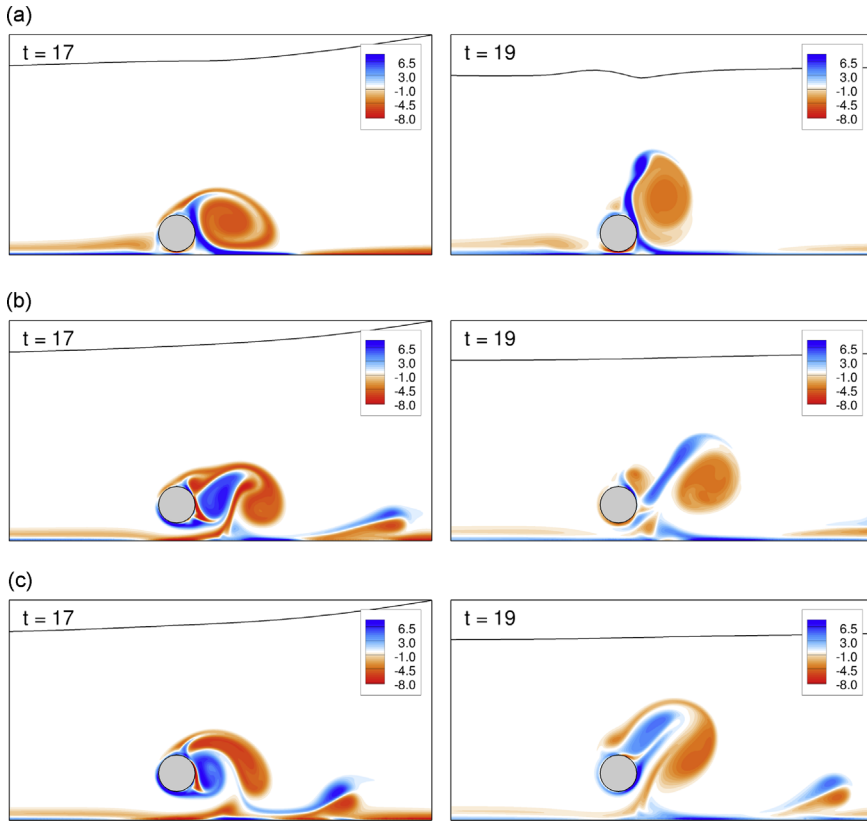


Fig. 14. Vorticity fields for $H/h = 0.5$ and various gap ratios. (a) $G/D = 0.1$. (b) $G/D = 0.5$. (c) $G/D = 0.8$.

When the gap height becomes larger, as seen in the cases of $G/D = 0.5$ and 0.8 , the interaction between the shear layer from the cylinder and that from the seabed becomes less. In the case of $G/D = 0.5$, the primary and secondary vortices act like a vortex dipole when the wave crest is away from the cylinder, which is similar to the case of $G/D = 0.3$. When the gap ratio becomes $G/D = 0.8$, the secondary vortex stretches out along the seabed completely without cut off by the negative vorticity. As a result, the positive vorticity in the vortex dipole weakens when the wave crest is away from the cylinder.

6.2.2. Effect of wave height

To understand the influence of the increased wave height on the formation of vortices, here the computational results of the vorticity fields induced by different wave height with the gap-to-diameter ratio $G/D = 0.1, 0.5$ and 0.8 are presented, as shown in Fig. 14 for $H/h = 0.5$ and Fig. 15 for $H/h = 0.7$. The increased wave height enhances the strength of vortices. As a result, the disturbance of the free surface by the vortices becomes pronounced for larger incident wave height.

In the cases of $G/D = 0.1$, because the gap ratio is very small, the vorticity fields of different wave heights exhibit similar patterns. In the cases of $G/D = 0.5$ and 0.8 , if the wave height is not very large, e.g. $H/h = 0.5$, the recirculation zones remain close to the cylinder and then move downstream. If the wave height is very large, e.g. $H/h = 0.7$, the primary vortex is very strong and then moves farther downstream when the wave crest is away.

In all cases, the generated vortices become well developed when the wave crest is away from the cylinder. These vortices do not significantly affect the crest of solitary waves, but have influence on the forces exerted on the cylinder.

6.3. Forces exerted on the cylinder

First of all, the time history of pressure, friction and total drag exerted on the cylinder for $H/h = 0.3$ and $G/D = 0.1$ is presented in Fig. 16 to clarify the importance of the components of drag. This result shows that because of large Re , the friction drag is relatively small compared to the pressure drag.

Fig. 17 illustrates the time history of drag and lift coefficients for $H/h = 0.3$ and $G/D = 0.1, 0.2, 0.3, 0.5, 0.8$ and 1.0 . It shows that when $G/D \geq 0.8$, the gap height is large enough so that there is no significant interplay between the separating shear layers generated from the cylinder and from the seabed, as shown in Fig. 13(d). Consequently, drag, and lift in particular, reduce obviously. Lift is significantly affected by the gap height. If the gap height becomes smaller, vorticity flux in the gap is suppressed, and the pressure on the seabed-side surface of the cylinder increases. The fluctuations in drag and lift after $t=17$ are caused by the motion of the separated vortices behind the cylinder.

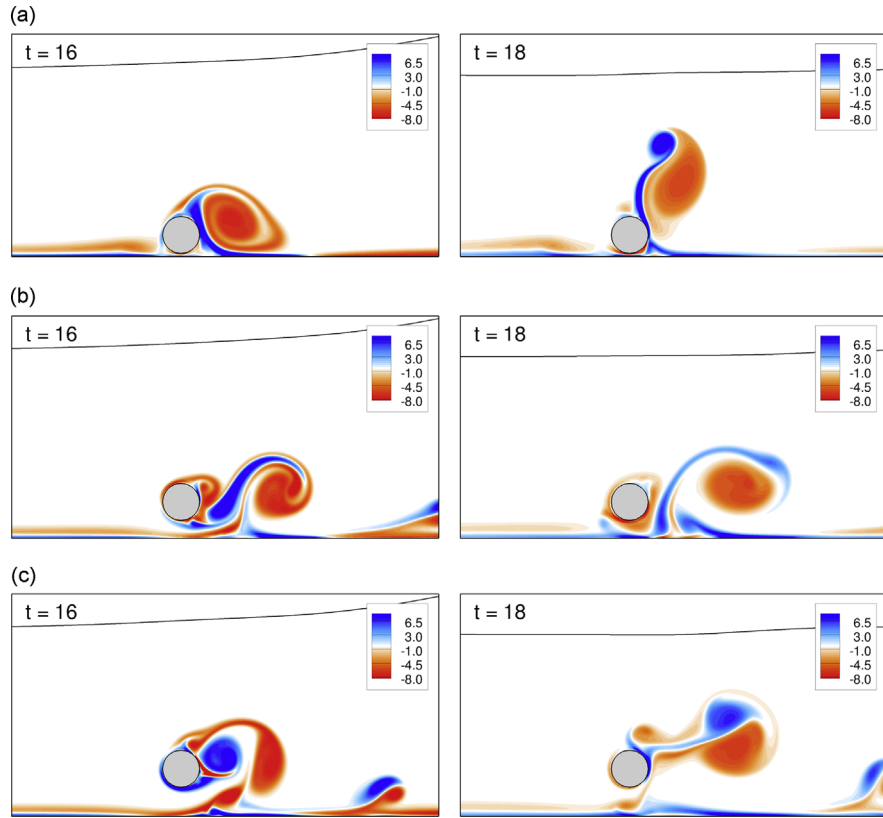


Fig. 15. Vorticity fields for $H/h = 0.7$ and various gap ratios. (a) $G/D = 0.1$. (b) $G/D = 0.5$. (c) $G/D = 0.8$.

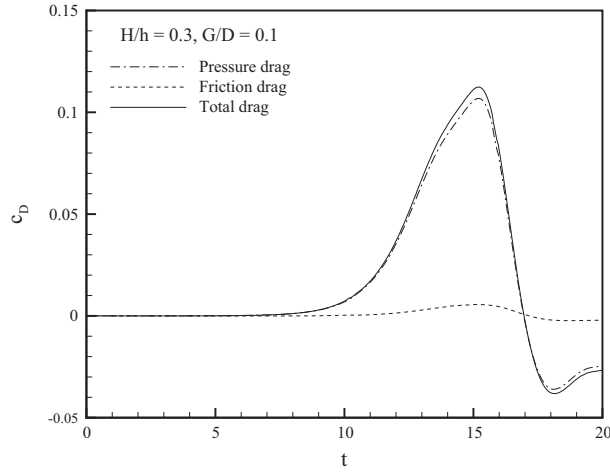


Fig. 16. Form and skin drag coefficient of the circular cylinder for $H/h = 0.3$ and $G/D = 0.1$.

[Fig. 18](#) shows the drag and lift coefficients for $H/h = 0.3\text{--}0.7$ and $G/D = 0.1, 0.5$ and 0.8 . [Fig. 19](#) illustrates the maximum drag and lift under different conditions. In [Fig. 19\(b\)](#) the positive and negative maxima of lift are illustrated separately. The maximum drag and lift increase linearly with H/h . Larger wave has faster speed, so that its maximum drag and lift appear earlier. If the gap height becomes very small, e.g. $G/D = 0.1$, the maximum drag and the positive maximum lift increase significantly, and the negative maximum lift becomes relatively small.

[Fig. 20](#) shows the time history of the resultant force and its position on the cylinder for $G/D = 0.1, 0.5$ and 0.8 (for the definition of β , see [Fig. 1](#)). [Figs. 21](#) and [22](#) illustrate the time evolution of instantaneous distributions of $p - p_0$ and resultant

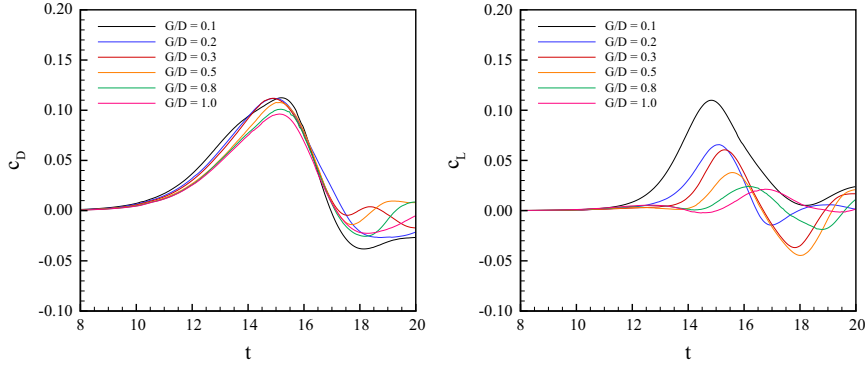


Fig. 17. Drag and lift coefficients of the circular cylinder for $H/h = 0.3$ and the indicated G/D ratios.

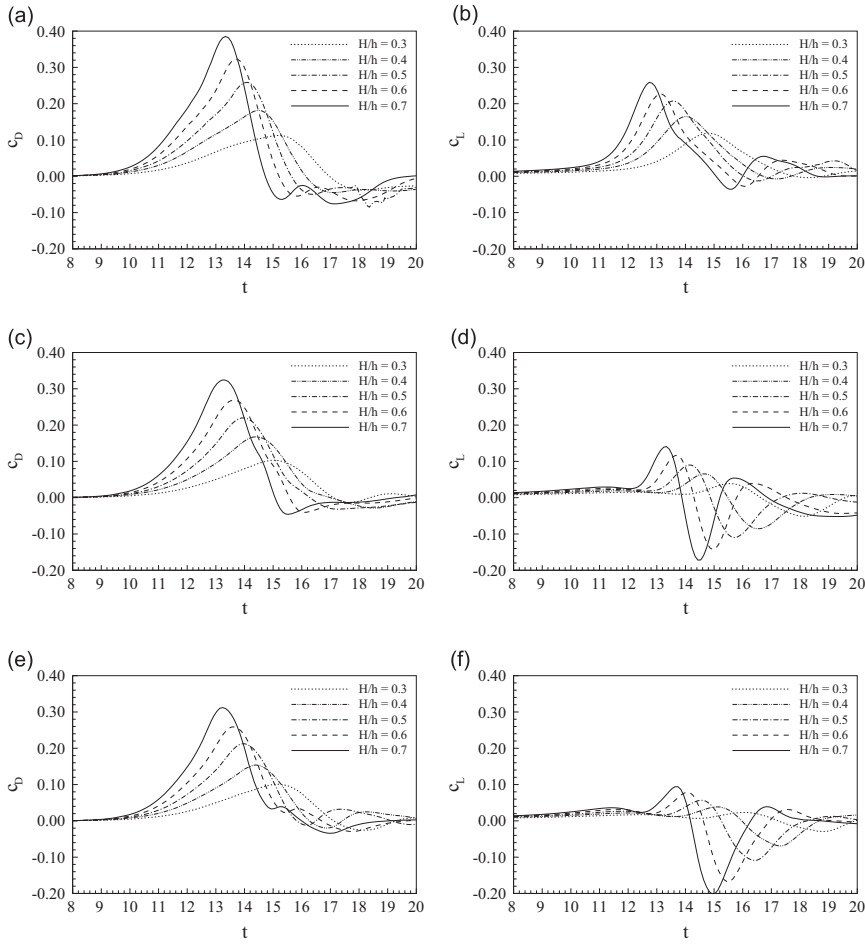


Fig. 18. Drag and lift coefficients of the circular cylinder for different wave heights. (a) and (b) $G/D = 0.1$. (c) and (d) $G/D = 0.5$. (e) and (f), $G/D = 0.8$.

forces for $H/h = 0.3$ and 0.7, respectively. Here p_0 indicates the pressure on the cylinder surface at $\beta=0$. The maximum resultant forces and their positions under different conditions are shown in Fig. 23. Like the behavior of drag and lift, c_T increases linearly with H/h . If the cylinder is in close proximity to the seabed, resultant force increases significantly. From Figs. 12 and 20, it can be found that the resultant force reaches to its maximum when the water level above the cylinder is approaching 85% of the maximum level.

From the pressure distributions shown in Figs. 21 and 22, it can be observed that placing the cylinder nearer the seabed generally increases the pressure on the seabed-side surface of the cylinder. To understand the effect of gap height on the

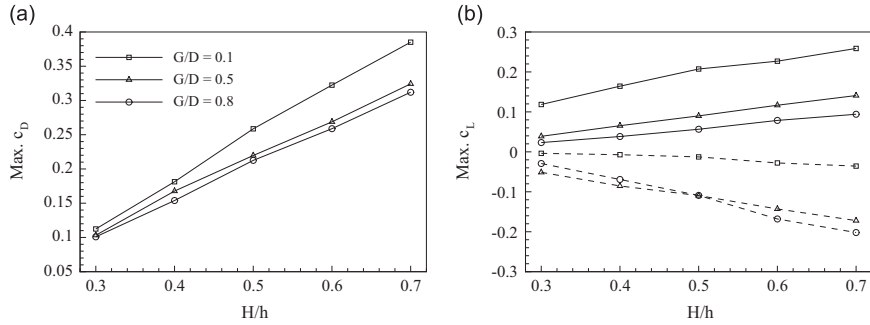


Fig. 19. Maximum drag coefficient of the circular cylinder for various H/h and G/D ratios.

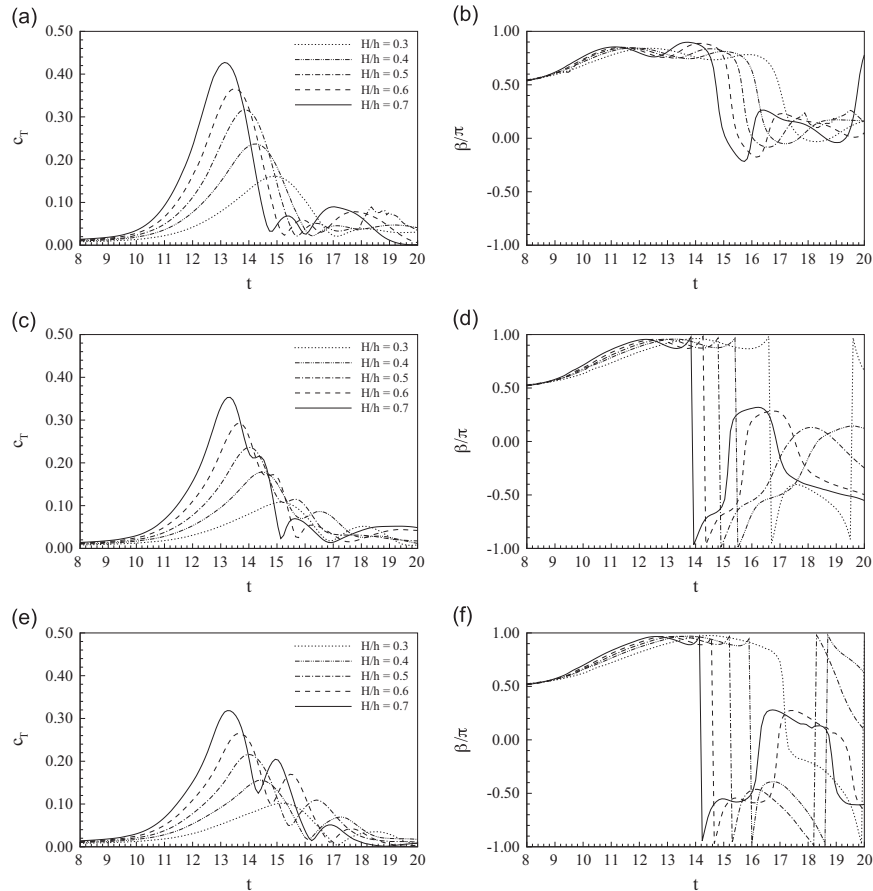


Fig. 20. Resultant force and its position on the circular cylinder for different wave heights. (a) and (b) $G/D = 0.1$. (c) and (d) $G/D = 0.5$. (e) and (f) $G/D = 0.8$.

forces, the time evolutions of the distributions of vorticity flux and pressure on the cylinder surface for $G/D = 0.1$ and 0.8 under different H/h values are shown in Figs. 24–27. As shown in (34), vorticity flux can be regarded as the source of pressure gradient. In the case of a smallest gap height ($G/D = 0.1$), when the wave crest is approaching the cylinder, vorticity is mainly generated from the regions between $0^\circ \leq \beta \leq 90^\circ$ and $250^\circ \leq \beta \leq 300^\circ$. The trend of vorticity flux leads to a negative pressure gradient from $\beta=0^\circ$ to 70° and a positive pressure gradient from $\beta=250^\circ$ to 300° . In the region $300^\circ \leq \beta \leq 360^\circ$, i.e., the region below the stagnation point, vorticity flux becomes very small, and the pressure gradient remains almost zero. Correspondingly, in the case of a largest gap height ($G/D = 0.8$), vorticity flux is generated from $0^\circ \leq \beta \leq 90^\circ$ and $270^\circ \leq \beta \leq 360^\circ$ when the wave crest is approaching the cylinder, showing an antisymmetric trend. As a result, smaller gap height leads to larger resultant force and smaller β value. In the cases of a largest gap height, the

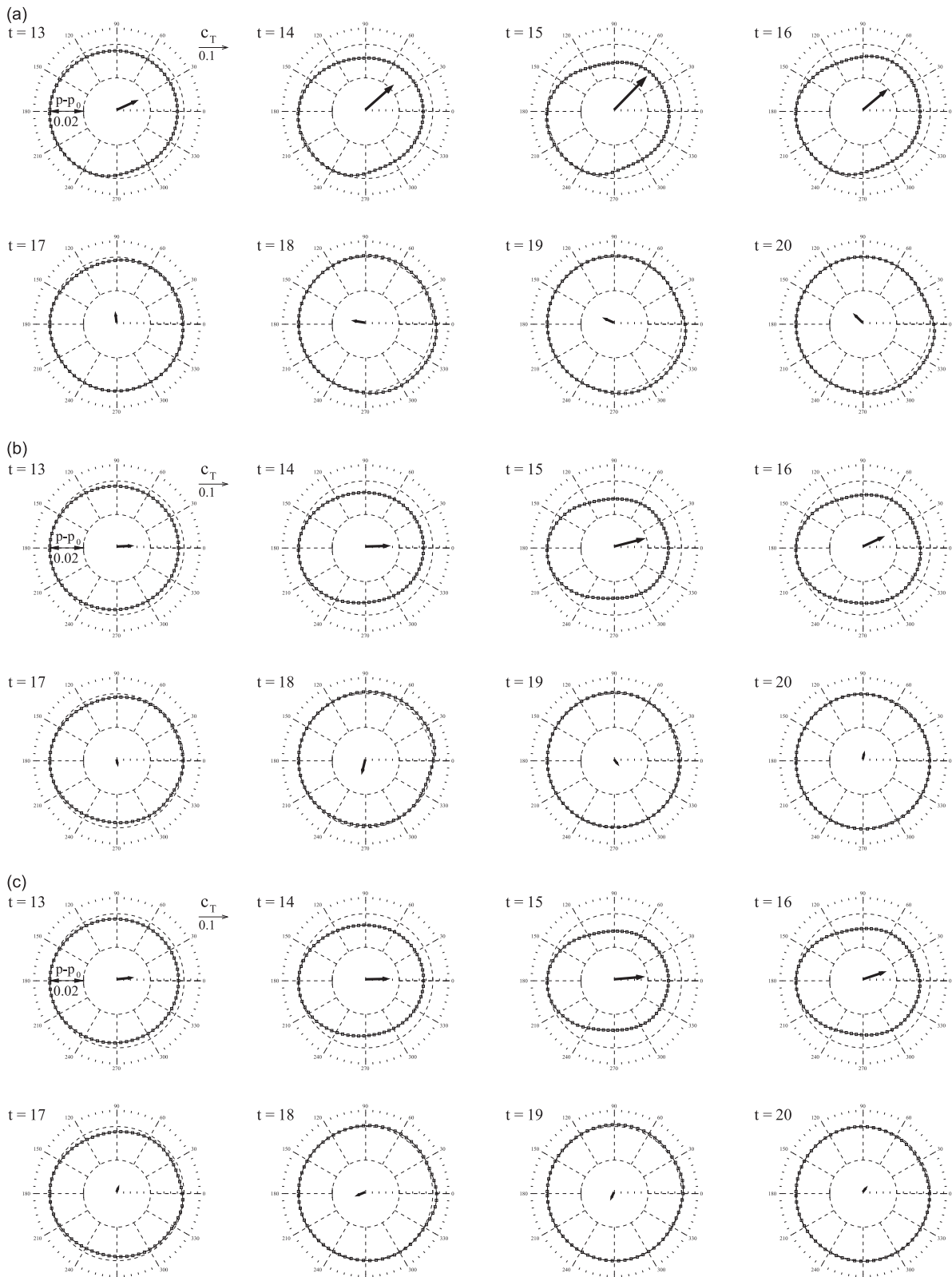


Fig. 21. Time evolution of instantaneous pressure distributions and resultant forces for $H/h = 0.3$ and various G/D values. (a) $G/D = 0.1$. (b) $G/D = 0.5$. (c) $G/D = 0.8$.

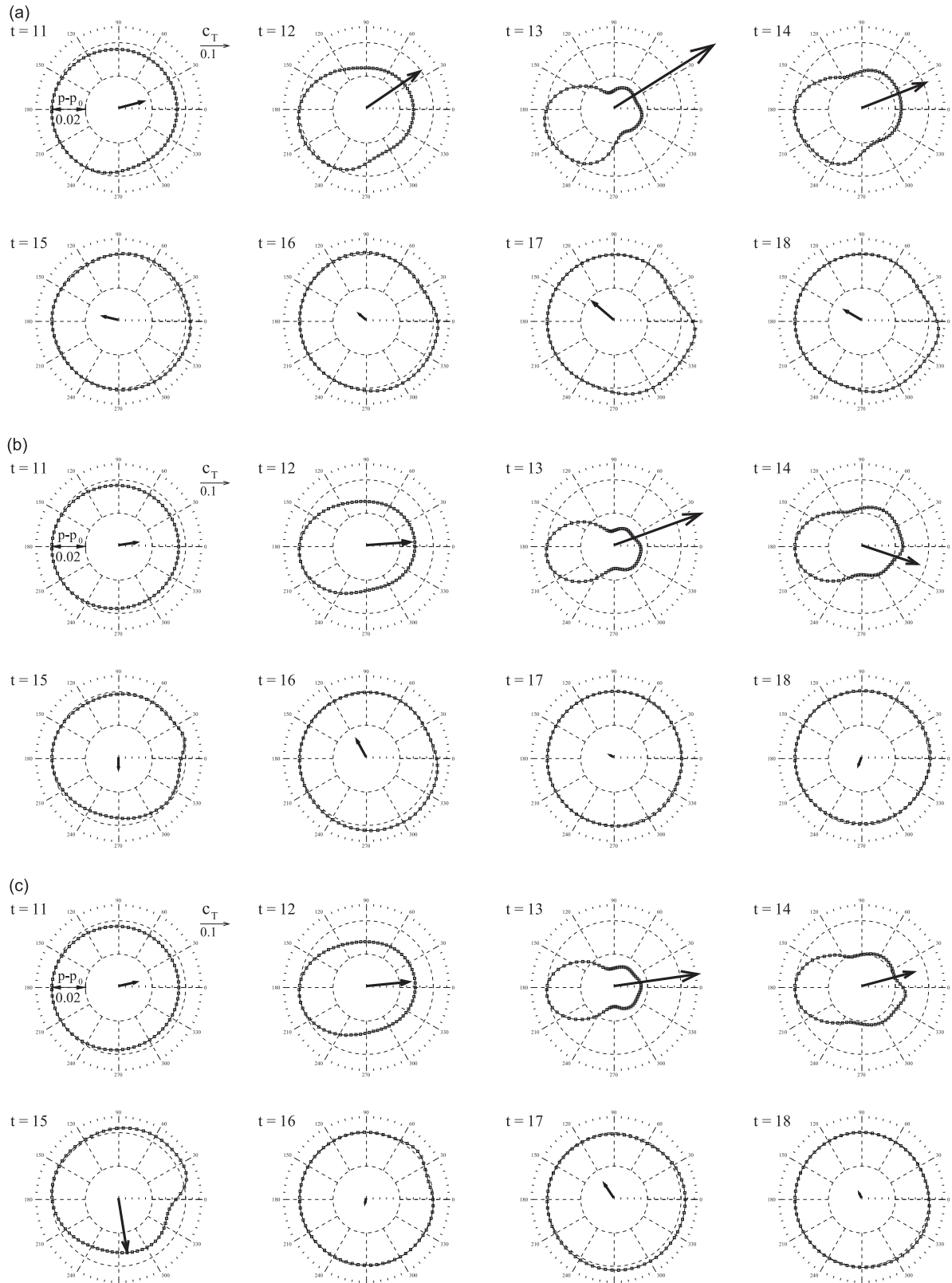


Fig. 22. Time evolution of instantaneous pressure distributions and resultant forces for $H/h = 0.7$ and various G/D values. (a) $G/D = 0.1$. (b) $G/D = 0.5$. (c) $G/D = 0.8$.

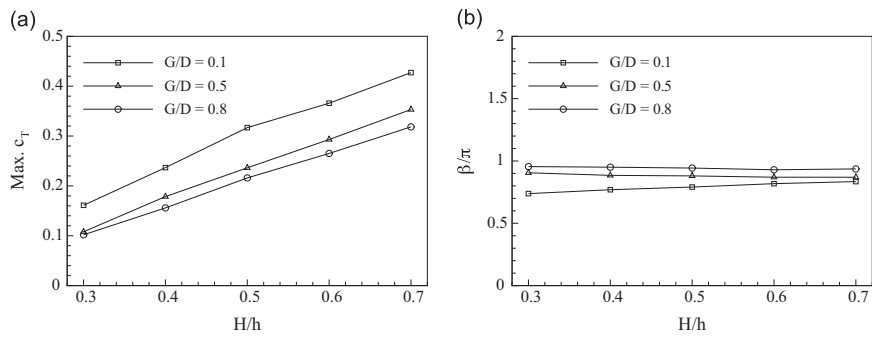


Fig. 23. Maximum resultant force and its position on the circular cylinder for various H/h and G/D ratios.

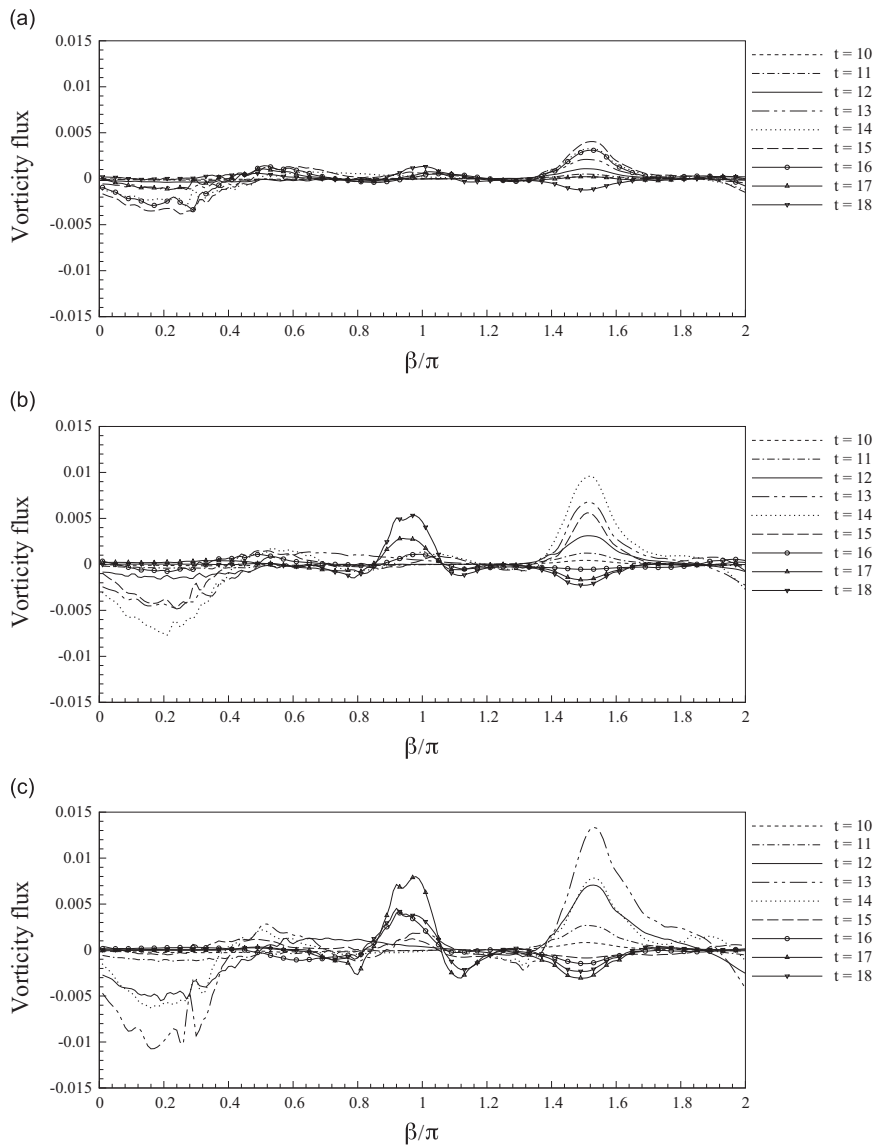


Fig. 24. Vorticity flux ($\nu \partial \omega / \partial n$) on the cylinder surface for $G/D = 0.1$ and different H/h values. (a) $H/h = 0.3$. (b) $H/h = 0.5$. (c) $H/h = 0.7$.

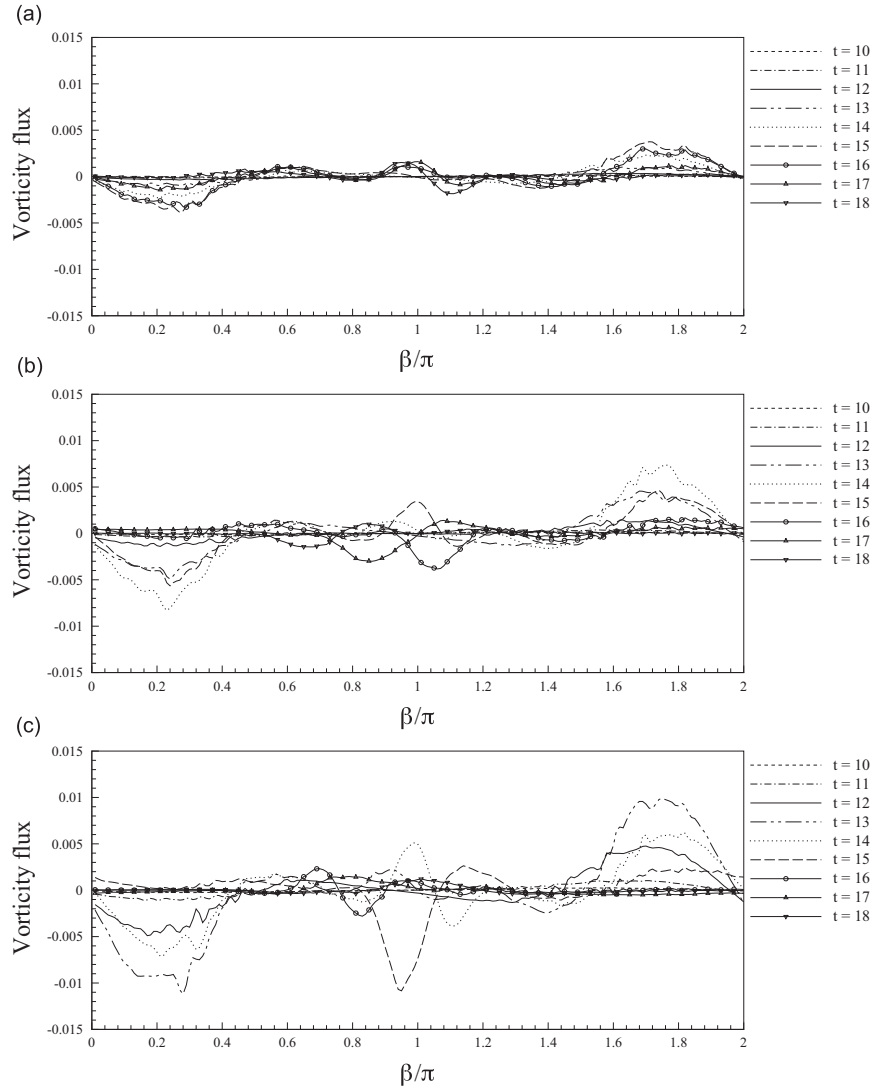


Fig. 25. Vorticity flux ($\nu \partial \omega / \partial n$) on the cylinder surface for $G/D = 0.8$ and different H/h values. (a) $H/h = 0.3$. (b) $H/h = 0.5$. (c) $H/h = 0.7$.

maximum forces point to the right. In the cases of a smallest gap height, the maximum forces point to the upper right, especially under a smaller wave height. When the wave crest moves away from the cylinder, the interaction of the separated vortices and the cylinder induces additional vorticity flux in the region $140^\circ \leq \beta \leq 220^\circ$, causes pressure gradient, and then leads to a drop in the curve of lift, as shown in Fig. 18. This phenomenon is more pronounced if the height of the incident wave is larger.

7. Summary

In this research, two-dimensional flow around a circular cylinder placed at various heights above a plane boundary and exposed to a solitary wave is investigated numerically, by using a generalized vortex method. This method is accomplished by employing the Helmholtz decomposition theorem, which decomposes velocity field into its irrotational and rotational components. The separating shear layers that cause the generation of vortices are confined inside small regions around the submerged circular cylinder. Owing to the essentially grid-free nature of the Lagrangian vortex methods, this model is capable of capturing the details of shear layer separation and vortex formation in relatively high resolution, even if the vortical flow is confined in compact regions.

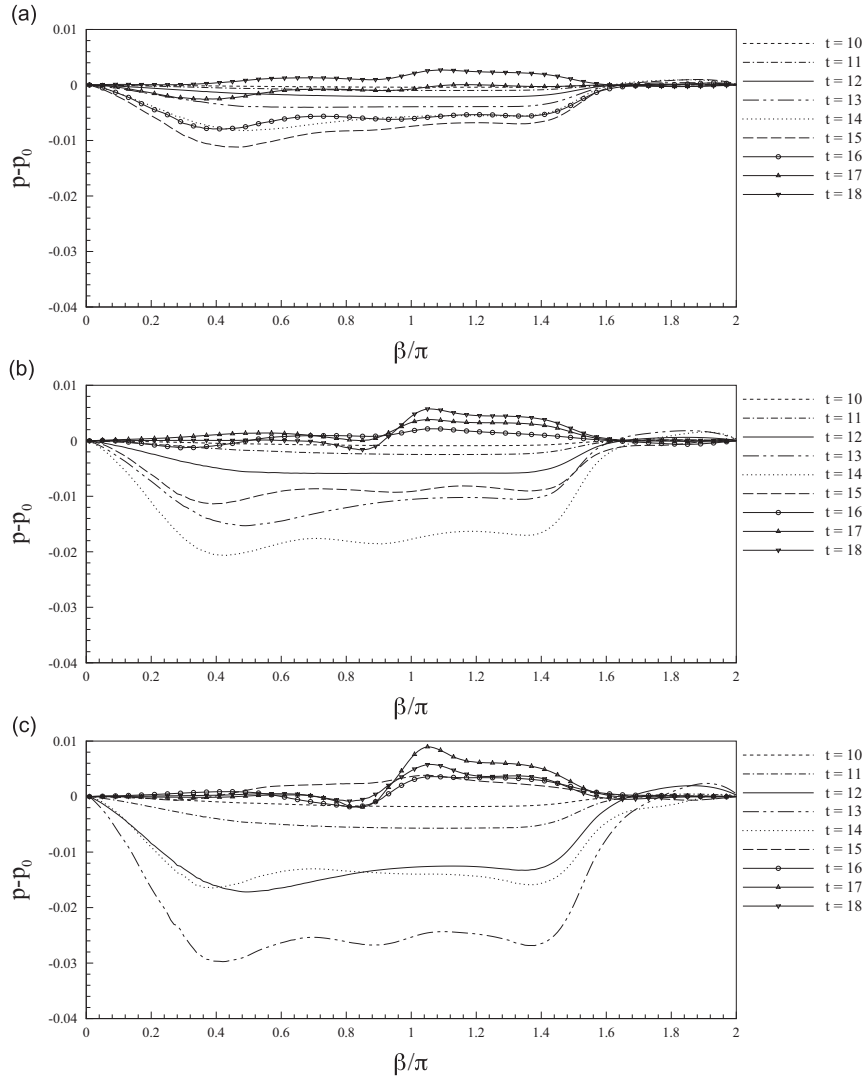


Fig. 26. Pressure distribution on the cylinder surface for $G/D = 0.1$ and different H/h values. (a) $H/h = 0.3$. (b) $H/h = 0.5$. (c) $H/h = 0.7$.

The main object of this research is to gain insight into the effects of the gap-to-diameter ratio and wave height on the vorticity dynamics and on the forces induced by the solitary wave over the cylinder, in view of its application to marine pipelines exposed to surface waves. The main results are summarized as follows.

- Around the cylinder the effect of vortices plays an important role on the flow field and should not be ignored. The strong shear flow near the seabed may cause significant pressure gradient and shear stress on the seabed, which may induce local scour in the vicinity of the cylinder.
- If the cylinder is placed at a small gap height, a single recirculation zone forms in the wake, and vortex shedding is suppressed by the effect of the seabed. If the gap height is larger, the secondary vorticity generated from the sea-bed side surface of the cylinder becomes more obvious, and significantly affects the formation of the primary recirculation zone.
- Placing the cylinder nearer the seabed increases the pressure on the wall-side surface of the cylinder. As a result, drag, positive lift and total force increase significantly if the cylinder is in close proximity to the seabed.
- When the gap height becomes larger, the pressure on the seabed-side surface of the cylinder decreases, and the shear layer from the gap interferes with the development of the main recirculating region behind the cylinder. These phenomena cause a reduction of the resultant force exerted on the cylinder.
- The maxima of drag, lift and total force increase linearly with the height of the incident wave.

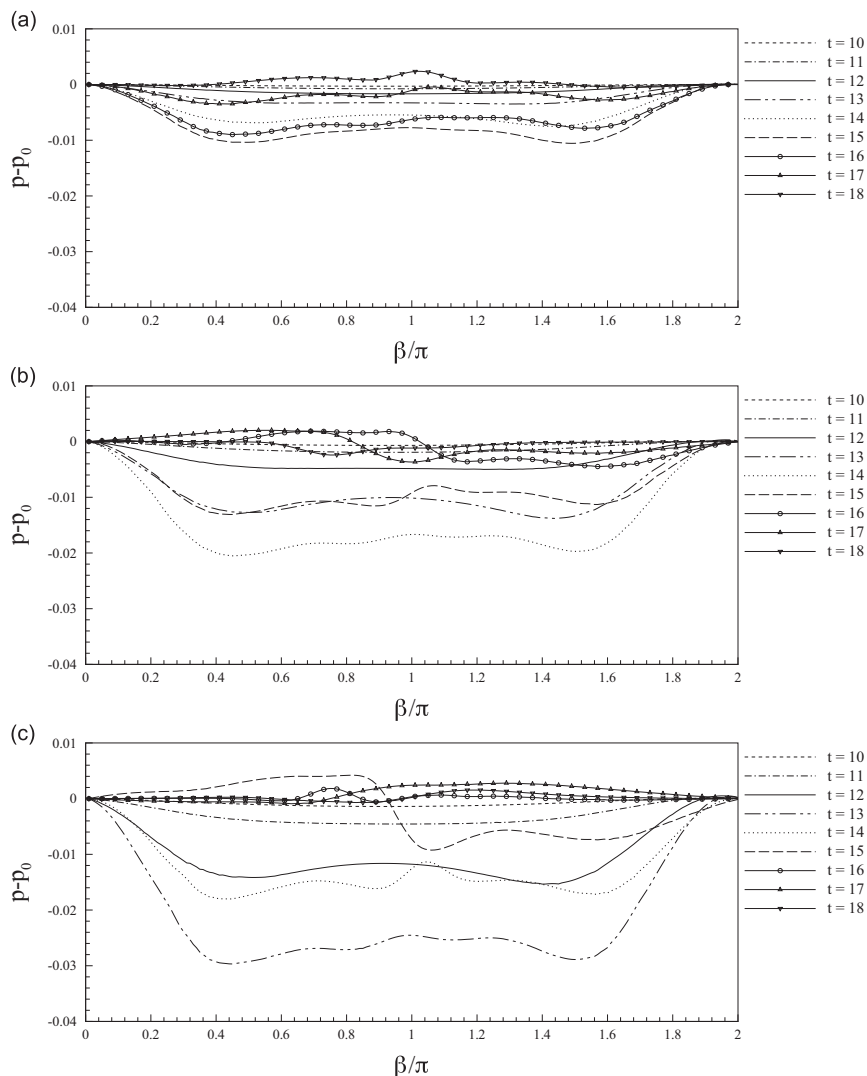


Fig. 27. Pressure distribution on the cylinder surface for $G/D = 0.8$ and different H/h values. (a) $H/h = 0.3$. (b) $H/h = 0.5$. (c) $H/h = 0.7$.

In this research, the flows simulated are two-dimensional. Three-dimensional flow occurs if the gap height or the incident wave becomes larger. Three-dimensional effects on vortex patterns and forces may be studied in the future.

Acknowledgement

This work was supported by the National Science Council of the Republic of China, Taiwan, under Contract no. NSC100-2221-E-033-019. The authors would like to thank three anonymous reviewers and the editors for their comments.

References

- An, H., Cheng, L., Zhao, M., 2011. Steady streaming around a circular cylinder near a plane boundary due to oscillatory flow. *Journal of Hydraulic Engineering* 137 (1), 23–33.
- Baker, G.R., Meiron, D.I., Orszag, S.A., 1982. Generalized vortex methods for free-surface flow problems. *Journal of Fluid Mechanics* 123, 477–501.
- Bouard, R., Coutanceau, M., 1980. The early stage of development of the wake behind an impulsively started cylinder for $40 < Re < 10^4$. *Journal of Fluid Mechanics* 101 (3), 583–607.
- Chang, C.C., Chern, R.L., 1991. A numerical study of flow around an impulsively started circular cylinder by a deterministic vortex method. *Journal of Fluid Mechanics* 233, 243–263.
- Chiew, Y.-M., 1990. Mechanics of local scour around submarine pipelines. *Journal of Hydraulic Engineering* 116 (4), 515–529.
- Cooker, M.J., Peregrine, D.H., Vidal, C., Dold, J.W., 1990. The interaction between a solitary wave and a submerged semicircular cylinder. *Journal of Fluid Mechanics* 215, 1–22.
- Cottet, G.H., 1996. Artificial viscosity models for vortex and particle methods. *Journal of Computational Physics* 127, 299–308.

- Degond, P., Mas-Gallic, S., 1989. The weighted particle method for convection-diffusion equations. Part 1: the case of an isotropic viscosity. *Mathematics of Computation* 53 (188), 485–507.
- Dipankar, A., Sengupta, T.K., 2005. Flow past a circular cylinder in the vicinity of a plane wall. *Journal of Fluids and Structures* 20 (3), 403–423.
- Koumoutsakos, P., Leonard, A., 1995. High-resolution simulations of the flow around an impulsively started cylinder using vortex methods. *Journal of Fluid Mechanics* 296, 1–38.
- Koumoutsakos, P., Leonard, A., Pepin, F., 1994. Boundary conditions for viscous vortex methods. *Journal of Computational Physics* 113 (1), 52–61.
- Li, F., Cheng, L., 1999. Numerical model for local scour under offshore pipelines. *Journal of Hydraulic Engineering* 125 (4), 400–406.
- Liang, D.F., Cheng, L., 2005. Numerical modeling of flow and scour below a pipeline in currents—Part I. Flow simulation. *Coastal Engineering* 52 (1), 25–42.
- Lin, C., Lin, W.J., Lin, S.S., 2005. Flow characteristics around a circular cylinder near a plane boundary. In: 16th International Symposium on Transport Phenomena, pp. 1–9.
- Lin, M.-Y., Huang, L.-H., 2009. Study of water waves with submerged obstacles using a vortex method with Helmholtz decomposition. *International Journal for Numerical Methods in Fluids* 60 (2), 119–148.
- Longuet-Higgins, M.S., Cokelet, E.D., 1976. The deformation of steep surface waves on water. I. A numerical method of computation. *Proceedings of the Royal Society of London. A. Mathematical and Physical Sciences* 350 (1660), 1–26.
- Longuet-Higgins, M.S., Fox, M.J.H., 1996. Asymptotic theory for the almost-highest solitary wave. *Journal of Fluid Mechanics* 317, 1–19.
- Lundgren, T., Koumoutsakos, P., 1999. On the generation of vorticity at a free surface. *Journal of Fluid Mechanics* 382, 351–366.
- Marshall, J.S., 2001. Inviscid Incompressible Flow. Wiley-Interscience, New York.
- Monaghan, J.J., 1985. Extrapolating B-splines for interpolation. *Journal of Computational Physics* 60 (2), 253–262.
- Ploumhans, P., Winckelmans, G.S., 2000. Vortex methods for high-resolution simulations of viscous flow past bluff bodies of general geometry. *Journal of Computational Physics* 165, 354–406.
- Qi, E.R., Li, G.Y., Li Wei, W.J., Wu, J., Zhang, X., 2006. Study of vortex characteristics of the flow around a horizontal circular cylinder at various gap-ratios in the cross-flow. *Journal of Hydrodynamics* 18 (3), 334–340.
- Rao, A., Thompson, M.C., Leweke, T., Hourigan, K., 2013. The flow past a circular cylinder translating at different heights above a wall. *Journal of Fluids and Structures* 41, 9–21.
- Smith, P.A., Stansby, P.K., 1988. Impulsively started flow around a circular cylinder by the vortex method. *Journal of Fluid Mechanics* 194, 45–77.
- Sumer, B.M., Jensen, B.L., Fredsøe, J., 1991. Effect of a plane boundary on oscillatory flow around a circular cylinder. *Journal of Fluid Mechanics* 225, 271–300.
- Tryggvason, G., 1988. Numerical simulations of the Rayleigh-Taylor instability. *Journal of Computational Physics* 75 (2), 253–282.
- Wu, J.Z., Wu, X.H., Ma, H.Y., Wu, J.M., 1994. Dynamic vorticity condition: theoretical analysis and numerical implementation. *International Journal for Numerical Methods in Fluids* 19 (10), 905–938.